Aerosol Science and Technology

ISSN: (Print) (Online) Journal homepage: www.tandfonline.com/journals/uast20

Capability and efficiency of droplets in removing nanoparticle contaminants from Si wafer via high-speed microdroplet impaction

Jinhyo Park, Seungwook Lee, Jeonggeon Kim & Donggeun Lee

To cite this article: Jinhyo Park, Seungwook Lee, Jeonggeon Kim & Donggeun Lee (2024) Capability and efficiency of droplets in removing nanoparticle contaminants from Si wafer via high-speed microdroplet impaction, Aerosol Science and Technology, 58:9, 1008-1023, DOI: 10.1080/02786826.2024.2338523

To link to this article: https://doi.org/10.1080/02786826.2024.2338523

AEROSOL SCIENCE AND TECHNOLOGY
2024, VOL. 58, NO. 9, 1008–1023
https://doi.org/10.1080/02786826.2024.2338523

Capability and efficiency of droplets in removing nanoparticle contaminants from Si wafer via high-speed microdroplet impaction

Jinhyo Park[†], Seungwook Lee[†], Jeonggeon Kim, and Donggeun Lee

School of Mechanical Engineering, Pusan National University, Busan, South Korea

ABSTRACT

The high-speed impact of liquid microdroplets has emerged as a promising method to eliminate nanoparticle contaminants from semiconductor wafer surfaces. However, existing experimental studies have primarily focused on evaluating their own nozzles for removing particles larger than 50 nm, which does not align with the current research roadmap where the target particles' size decreases down to sub-10 nm. As it is more challenging to remove smaller particles, there is a strong need to better understand droplet's spreading behavior in relation to the detachment of particles from a surface. Nonetheless, there remains a lack of experimental evidence to validate existing models or a scarcity of numerical simulation studies, mainly due to the practical difficulties associated with single droplet experiments. Hence, in this study, we conduct a series of numerical simulations to investigate the time-dependent spreading behavior of the droplet, together with collecting local velocity data at the attached particle position. The local velocity data is then integrated to an existing model to predict the effective cleaning diameter for each impact condition. Starting from the free-fall dropwise impaction, we develop a single-microdroplet cleaning system by minimizing the number of sprayed droplets and capturing their behavior using a high-speed camera (HSC), with aims of validating the model predictions and numerical simulations. Finally, we provide a contour plot for a prior prediction of the effective cleaning diameter from the impaction conditions of microdroplets.

ARTICLE HISTORY
Received 29 December 2023
Accepted 18 March 2024

EDITOR
Jonathan P. Reid

1. Introduction

Inorganic, organic, metallic, nonmetallic, and polymer particles unintentionally generated during the semiconductor manufacturing processes are known to contaminate the target surface. This contamination represents a significant factor contributing to the reduced yield of semiconductor devices (Hong et al. 2019). Methods for eliminating these contaminants are primarily categorized into chemical cleaning methods and physical cleaning methods (Kern 1990). Chemical cleaning methods are problematic due to their use of toxic chemicals. Moreover, when the line width (also known as the feature size that measures the width of the smallest lines that can be patterned) in a semiconductor fabrication process is smaller than 10 nm, the high aspect ratio (i.e., height to thickness) of the line pattern hinders the ultrapure water-based cleaning solution from reaching the bottom of the pattern (Cho et al. 2020). Therefore, physical cleaning methods are currently receiving increased attention, as they facilitate contaminant removal through momentum exchange caused by the impact of a less toxic solution on the surface. This approach results in fewer environmental and health concerns (Okorn-Schmidt et al. 2014; Henry and Minier 2014).

When a fluid flows rapidly over a contaminated wafer surface, the resulting momentum exchange with surface contaminants generates several forces: a drag force, a lift force, and a torque. These forces collectively contribute to the detachment and removal of contaminants, involving sliding, lifting, and rolling processes. Among these forces, rolling induced by drag force is recognized as the dominant factor in the removal of nanoparticles (Zoeteweij, Van der Donck, and Versluis 2009). However, when a pressurized gas is employed, the gas's lower density and viscosity, in comparison to liquids, result in insufficient drag forces acting on nanometer-sized contaminant

---

CONTACT Donggeun Lee donglee@pusan.ac.kr School of Mechanical Engineering, Pusan National University, Busandaehak-ro 63beon-gil, 2, Geumjeong-gu, ME bldg. Room No 517, Busan, 46241, South Korea.

[†]Both authors contributed equally to this paper.

Supplemental data for this article can be accessed online at https://doi.org/10.1080/02786826.2024.2338523.

particles, leading to reduced particle removal efficiency. To address this challenge, current research endeavors are actively exploring the utilization of high-speed spraying of liquids. This approach aims to enhance particle removal efficiency while minimizing the consumption of ultrapure water.

When a droplet impacts the surface perpendicularly at a velocity of U, it initially spreads across the surface, forming a circular film. The radial spreading velocity of this liquid film is highest immediately after the impact, gradually decreasing as the spreading process continues. Eventually, the liquid film ceases to spread, reaching its maximum spreading diameter ($D_{\max}$). Numerous studies have been conducted on dropwise impaction, and the key findings of relevant previous studies have been summarized comparatively in Table 1. It is worth noting that most prior studies in Table 1 have focused on predicting $D_{\max}$ under various impaction conditions. This was accompanied by normalizing $D_{\max}$ with the initial droplet diameter (D_0), denoted as the maximum spreading ratio ($\beta_{\max} \equiv D_{\max}/D_0$), and expressing $\beta_{\max}$ as a function of Weber number (We) and Reynolds number (Re). Here, We is a dimensionless number representing the ratio of the impaction kinetic energy of the droplet to surface tension, while Re represents the ratio of inertia to friction during liquid film spreading (Yonemoto and Kunugi 2017). For example, Pasandideh-Fard et al. (1996) proposed an equation for calculating the spreading velocity of the liquid film after droplet impact, relying on the principles of mass conservation and energy conservation. This work was subsequently followed by various model developments in Table 1. Notably, the majority of relevant experimental data originated from the impaction of millimeter-sized droplets under free fall conditions. These experiments involved high-speed camera measurements to track changes in liquid film diameter as a function of time (Pasandideh-Fard et al. 1996; Jung and Hutchings 2012; Yonemoto and Kunugi 2017; Tan 2017).

When it comes to removing nanoparticles attached to a solid surface, it should be noted that a significant velocity gradient occurs within the spreading liquid film due to the formation of a viscous boundary layer on the surface (Snow et al. 2013; Kondo & Ando, 2019). This effect is particularly pronounced when the target particle is small, leading to a substantial reduction in the local spreading velocity at the particle's position, which falls well below the (aforementioned) film spreading velocity or impaction velocity. Consequently, obtaining the relationship between the distribution of the local spreading velocity within the liquid film and the impact conditions of the droplet (such as its diameter and impaction velocity) is crucial for quantitatively predicting the feasibility of particle removal.

Due to the challenges associated with measuring the local spreading velocity of a thin liquid film, there have been no experimental studies conducted on this aspect. Even computational fluid dynamics (CFD) simulations for the purpose of particle removal have been quite scarce. Kondo and Ando (2019) carried out a CFD simulation on the impaction of droplets with diameters of 200 μm. Their aim was to determine the distribution of the local spreading velocity within a spreading droplet and calculate the resulting drag force acting on the particles. They subsequently presented a spatio-temporal evolution diagram to judge particle removal for three different impact velocities of droplet. However, their model has not been validated with experimental data, presumably due to practical difficulties in conducting single-droplet cleaning experiments. Indeed, as seen in Table 2, existing experimental studies have primarily focused on the ensemble effect on particle removal efficiency (PRE) through the multiple impaction of a large number of fine droplets (Zoeteweij, Van der Donck, and Versluis 2009; Seike et al. 2010; Iwasaki et al. 2015). Additionally, Table 2 highlights the current research trends, wherein smaller and higher-speed droplets are increasingly used, while the target particle sizes for

Table 1. Comparative review of previous research on the analysis of dropwise impaction, emphasizing model or CFD predictions, droplet sizes, impact velocities, and spreading dynamics.

Year	Authors	Model / CFD	Droplet size (mm)	Impact velocity (m/s)	Spreading velocity	$\beta_{\max}$	β(t)
1996	Pasandideh-Fard et al.	CFD	2.05	1	x	o	o
2002	Roisman et al.	Model	2.75 – 3.5	1.18 ∼ 4.5	o	o	o
2009	Wang et al.	Model	2.1 – 2.2	5.2 ∼ 5.3	x	o	o
2011	Hung et al.	Model	2.1 – 2.4	0.4 ∼ 1.4	o	o	o
2012	Jung & Hutchings	Model	0.025 – 0.028	3, 6, 8	x	o	o
2014	Riboux and Gordillo	Model	2	1.29 – 2.28	x	o	x
2017	Yonemoto and Kunugi	Model	1.2	0.44 – 3.7	x	o	o
2017	Choudhury et al.	Model	2.2 – 3.7	0.44 – 0.7	x	o	o
2012, 2015	Visser et al.	CFD & Model	0.05	50	x	o	o
2016	Lee et al.	CFD	2	0.2 – 3.6	o	o	o
2017	Xu et al.	CFD	2.05	0.44 – 3.7	x	o	o
2019	Liu et al.	CFD	2	1.1 – 2.4	x	x	x

Table 2. Previous studies on particle removal *via* physical cleaning, comparatively summarized in terms of detailing methods, droplet sizes, velocities, and particle removal efficiency.

Year	Author	Method	Droplet size (μm)	Droplet vel. (m/s)	Particle size (μm)	Type of impaction	Performance	Removal model
1994	Soltani and Ahmadi	Sim.	10–100	x	20,35[a]	Single	PRE[b]	Moment balance
2019	Kondo and Ando	Sim.	200	30,40,50	0.01	Single	AR[c]	Moment balance
2009	Zoeteweij et al.	Sim.& Exp.	27	x	>1	Single, Multiple	PRE 77–100%	Moment balance
2009	Xu et al.	Exp.	7–30	35–85	>0.065	Multiple	PRE 35–100%	–
2010	Seike et al.	Exp.	5–35	40–90	0.132	Multiple	PRE $<75\%$	Moment balance
2011	Sato et al.	Exp.	22,40	20–80	>0.078	Multiple	PRE $<35\%$	Impact Energy
2015	Iwasaki et al.	Exp.	2–38	40–100	>0.045	Multiple	PRE $\sim50\%$	Impact Energy

[a] Range of particle diameters that have been validated with experimental data.
[b] PRE: Particle removal efficiency based on the count of particles before and after cleaning.
[c] AR: Ratio of effective cleaning area to the maximum spreading area of liquid film.

cleaning wafer surfaces have decreased in recent years. According to the ITRS front surface preparation roadmap (Snow et al. 2013), the critical particle diameter has annually decreased down to sub-10 nm. Since it is more challenging to remove smaller particles from a surface (Snow et al. 2013), there is a strong need to establish the intrinsic limits of high-speed microdroplet impaction for removing the smallest particles, based on single-droplet experiments.

In this study, therefore, we conducted a series of CFD simulations and single-droplet experiments. Initially, we performed CFD simulation to investigate the impact of a single microdroplet on a surface. The results were validated by comparing the $\beta_{\max}$ values with our experiments and values from previous literature. Specifically, we analyzed the time-dependent spreading behavior of the droplet to obtain the local velocity distribution inside the liquid film. This information was subsequently utilized in an existing model to calculate the drag force at the position of the target particle, the rotational moment, and consequently the effective cleaning diameter. We also developed a single-droplet cleaning system by minimizing the number of sprayed droplets and visualizing them through a high-speed camera (HSC). The measured effective cleaning diameters were directly compared with those obtained from CFD simulations to further validate the model.

2. Methods

2.1. Particle removal model

As depicted in Figure 1, when a single droplet with a diameter of D_0 impacts a smooth and dry wafer surface, the droplet transforms into a liquid film, rapidly spreading in the radial direction. The spreading velocity of the liquid film gradually decreases due to friction with the surface and the limited initial volume. The spreading stops when it reaches the maximum diameter, $D_{\max}$. When the spreading liquid film encounters a small particle attached to the surface, it generates a lift force (F_L), a drag force (F_D), and a rotational moment (M_D) around the particle. These forces serve as driving forces for detaching the particle from the surface, but they encounter resistance from opposing forces, such as the adhesion force (F_{ad}) and friction force (F_f). According to Zoeteweij, Van der Donck, and Versluis (2009), an attached particle would (1) detach perpendicularly when $F_L > F_{ad}$, (2) slide horizontally on the surface and eventually detach when $F_D > F_f$, or (3) rotate to detach when the moment imbalance ($\sum M > 0$) is achieved. The various forces described above depend on the properties of the surface, the size and properties of the droplet, and the size and properties of the particle which include its hardness or deformability that determines the contact radius (a) of the particle on the surface (Snow et al. 2013).

The adhesion force (F_{ad}) of a nanoparticle is typically approximated by the van der Waals force (F_{vdw}), which is calculated for a spherical particle using Equation (1), while neglecting its gravity force. F_{vdw} is a function of the Hamaker constant (A), the particle diameter (d_p), the particle-to-surface distance (z) (usually assumed to be 0.4 nm), and the contact radius (a) (Zoeteweij, Van der Donck, and Versluis 2009).

$$F_{vdw} = \frac{Ad_p}{12z^2}\left(1 + \frac{2a^2}{zd_p}\right) \tag{1}$$

Unlike a hard particle, which has nearly a point contact with the surface, a soft particle can deform on the surface to create a circular contact cross-section, potentially hindering particle detachment. Typically, the contact radius of a hard particle is estimated using the Derjaguin-Muller-Toporov (DMT) model, while that of a soft particle is estimated using the Johnson-Kendall-Roberts (JKR) model (Johnson, Kendall, and Roberts 1971; Derjaguin, Muller, and Toporov 1975). Since the JKR model tends to overestimate the van der Waals force (F_{vdw}) through the term of ‘a’

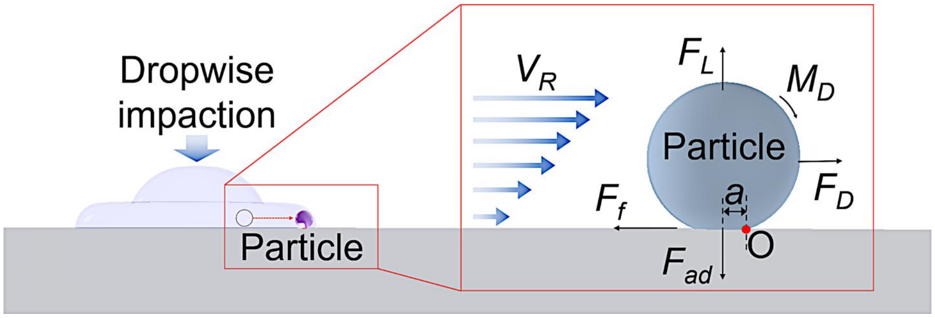

Figure 1. Illustration of the dropwise impaction and its resulting forces acting on a particle attached to a flat substrate.

compared to the DMT model, it can consequently underestimate the effects of external forces (F_d, F_L, and M_d) on particle removal. In this study, we applied the JKR model (Johnson, Kendall, and Roberts 1971) regardless of the particle hardness, as described in Equation (2).

$$a^3 = \frac{R}{K}\left[F + 3\pi\Delta\gamma R + \sqrt{6\pi\Delta\gamma RF + (3\pi\Delta\gamma R)^2}\right] \tag{2}$$

where R originally represents the combined radius of two contacting objects but is simply treated as the particle radius in this study, as the particle contacts a flat surface. F represents additional external forces, such as gravity force or electrostatic force, which contribute to increasing the F_{ad}. However, these forces are simply neglected with $F = 0$ in this study, given the small size of target particles and the loss of electrical charge in the water film. $\Delta\gamma$ represents the work of adhesion at the interface between the surface and the particle. K is the combined value of the Young's modulus of the two objects: particle and surface. When the Young's modulus of the particle is E_1 and that of the surface is E_2, K is calculated using Equation (3).

$$K = \frac{4}{3}\left[\frac{(1-\nu_1^2)}{E_1} + \frac{(1-\nu_2^2)}{E_2}\right]^{-1} \tag{3}$$

where ν is the Poisson ratio of the two objects.

The lift force (F_L) and the drag force (F_D) are calculated using Equations (4) and (5), respectively (Burdick, Berman, and Beaudoin 2005).

$$F_L = 1.62\eta d_p^2\left(\frac{\rho}{\eta}\frac{\partial u}{\partial y}\right)^{\frac{1}{2}} V_R \tag{4}$$

where η is the viscosity of the fluid, ρ is the density of the liquid, $\partial u/\partial y$ is the vertical gradient of the local spreading velocity u of the liquid, and V_R is the flow velocity at the center of the particle.

$$F_D = \frac{1}{2}\rho V_R^2 C_D A_p \tag{5}$$

where A_p ($= \pi d_p^2/4$) is the frontal area of the particle; C_D represents the drag coefficient of the spherical particle, which is calculated by Equation (6).

$$C_D = 1.7f = 1.7\frac{24}{Re_p} \tag{6}$$

where f is the friction factor, and Re_p is the Reynolds number based on the diameter of particle. The rotational moment (M_D) is calculated by Equation (7).

$$M_D = \frac{1}{2}\rho V_R^2 C_M V_p \tag{7}$$

where V_p is the particle volume, and the moment coefficient C_M is calculated by Equation (8) (Burdick, Berman, and Beaudoin 2005).

$$C_M = 0.944f = 0.944\frac{24}{Re_p} \tag{8}$$

By combining Equations (1), (4), (5), and (7), the moment equilibrium with reference to the point (O) in Figure 1 is assessed to determine particle detachment through Equation (9).

$$\sum M = M_D + 0.5F_D d_p - (F_{ad} - F_L)a > 0 \tag{9}$$

As such, $\sum M > 0$ can serve as a criterion for judging particle detachment from the surface by rotation at the point O. The point O is located at $x = a$, which is a distance equal to the contact radius (a) from the contact center. Clearly, the local velocity distribution (u) of liquid film is a key factor, being involved in the terms such as $\partial u/\partial y$ and V_R in Equations (4), (5), and (7), to evaluate the criterion. Precise measurement of $\partial u/\partial y$ and V_R at the center of nanoparticle, such as 10 nm away from the surface for the case of 20-nm particles, is practically impossible; therefore, CFD simulations were used for this purpose. For this study, all material properties involved in Equations (1)–(9) are listed in Table 3.

Table 3. Material properties used in the model calculations and subsequent CFD simulations.

Parameter	Value	Parameter	Value
Viscosity of water (η)[1]	8.89×10^{-4} Pa·s	Ti Young's modulus (E_1)[4]	110 GPa
Surface tension of water (σ)[1]	71.7×10^{-3} N/m	Si Young's modulus (E_2)[5]	125 GPa
Density of Water (ρ)[1]	997 kg/m^3	Ti Poisson's ratio (ν_1)[4]	0.36
Static contact angle (θ_0)[2]	28°	Si Poisson's ratio (ν_2)[5]	0.188
Density of Ti (ρ_P)[3]	4,540 kg/m^3	Hamaker constant (A)[6]	9.46×10^{-20} J
		Work of adhesion ($\Delta\gamma$)[7]	0.137 J/m^2

[1] Engineering ToolBox (2004); [2] Measured with a contact angle meter (SEO, Phoenix300); [3] Pierson (1999); [4] Hanson (1995); [5] Moram et al. (2006); [6] Bergström (1997); [7] You and Wan (2013); Referring to their paper, we estimated the work of adhesion ($\Delta\gamma$) between Ti particles and Si substrate by taking a geometric average of the surface energies of Ti and Si (0.21 J/m^2 and 0.09 J/m^2, respectively).

2.2. CFD simulations and validations for free-fall impaction of coarse droplet

The unsteady Volume of Fluid (VOF) method in the commercial CFD software (ANSYS Fluent 2020R1) was utilized to simulate the spreading behavior of a liquid droplet on a hydrophilic Si wafer. User-defined functions (UDF) were incorporated to introduce the dynamic contact angle (Voinov 1976; Wang et al. 2007) at the leading edge of the spreading liquid film. For the calculation, we used the Voinov model expressed as $\theta^3 = \theta_0^3 + 9Ca\left(\ln\left(\frac{h_0}{h_m}\right) - 1\right)$, where θ and θ_0 are the dynamic and static contact angle, respectively; Ca $(= \eta u/\sigma)$ is the Capillary number involving the surface tension of the liquid (σ); and the macroscopic length scale h_0 is approximated by D_0 while the limiting length scale h_m is of the order of 1 nm (Voinov 1976). To facilitate efficient calculations, we assumed axisymmetry with respect to the vertical central axis of the droplet upon impact. As shown in Figure S1, the (2-D) calculation domain was set to be sufficiently large to encompass the falling and spreading liquid droplet, adjusting its size in proportion to the droplet size. A non-uniform grid system was generated, specifically refining grids such that the grid size gradually increased by 1.2 times from a minimum size of $D_0/2000$ on the surface and the symmetric axis until $x \le 0.7D_0$ or $y \le 0.25D_0$; beyond this region, the size was set to $D_0/200$. Consequently, the minimum grid size decreased from micrometer to nanometer scales as droplet size was reduced to micrometers for the removal of nanoparticle.

A series of CFD simulations was initially performed for a 2 mm diameter water droplet with the material properties listed in Table 3. The impaction velocity (U) of the droplets was set between 0.45 and 1.45 m/s to replicate their free-fall conditions as described in the literature. Additionally, we conducted a free-fall impaction experiment using a 2 mm diameter water droplet, chosen for its ease of observation, to validate the simulation results. Figure 2a illustrates a schematic diagram of the experimental setup. A drop of deionized (D.I.) water was dispensed from a blunt-tip syringe needle (20-gauge) and fell onto a flat Si wafer due to gravity. The height of the needle tip was adjusted between 50 and 150 mm to align the impaction velocity of the drop with the simulation range (0.45 to 1.45 m/s, respectively). A high-speed camera (Photron Fastcam SA3, Japan) capturing at 30,000 frames per second recorded the instantaneous position of the droplet. These images were analyzed to measure the droplet's velocity and size just before impact. Following impact, the ongoing transformation of the droplet was continually monitored at the same frame rate until it ceased spreading.

Figure 2b displays a sequence of images showcasing the evolving droplet at four different times, ranging from 0.5 to 2.6 ms, depicted in black. These are compared with the simulated boundaries of the spreading liquid, highlighted by green dashed lines. As a result, the CFD simulations successfully track the continuously deforming boundary of the liquid film, providing accurate predictions of the instantaneous diameter of the liquid film and the resulting film spreading velocity throughout the dropwise impaction process. It is notable that at 2.6 ms, the experimental observation reveals a flat liquid film, while the CFD simulation depicts a pizza-like shape—a flat central part bordered by a thick crust. This discrepancy arises because the CFD simulation provides a cross-sectional boundary of the liquid, whereas the high-speed camera (HSC) captures a side view where the central part remains hidden. Despite this, the CFD predictions closely align with the experimental findings, showing differences within 6% regarding the diameter, thickness, and shape of the deforming liquid drop.

2.3. Single-microdroplet experiments for removal of nanoparticles from a Si wafer surface

Additional experiments were conducted to provide experimental evidence for the inherent capability of individual microdroplets in removing nanoparticles from a dry wafer surface. Firstly, we prepared a set of

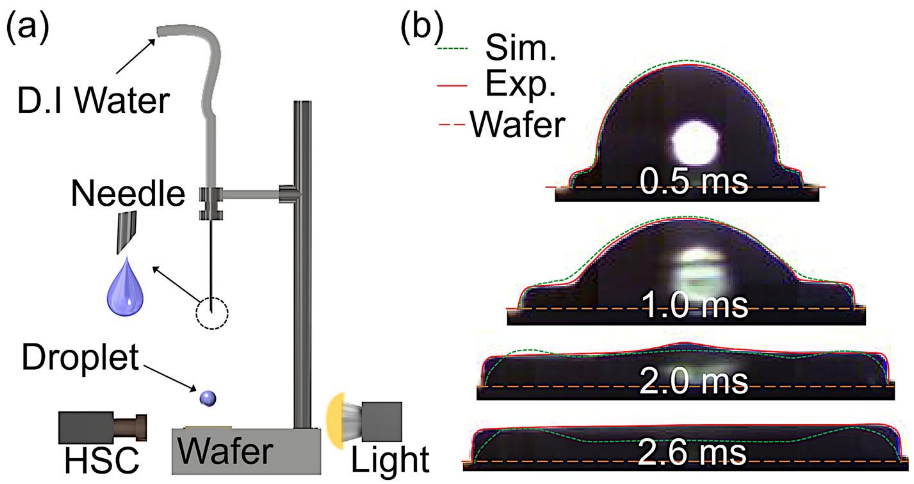

Figure 2. Free-fall dropwise impaction experiment with (a) a schematic diagram of experimental apparatus, and (b) the transient transformation of a coarse droplet with $D_0 = 2$mm after its impact with a velocity of 1.1 m/s, where its captured images were directly compared with CFD results.

uniformly contaminated wafer samples by depositing Ti nanoparticles onto the wafer surface. These Ti nanoparticles, with an average diameter of ∼20 nm, were produced using a home-made spark discharger (Lee et al. 2011). They were positively charged using a corona discharger (Ock et al. 2018) and subsequently deposited onto a 1 cm x 1 cm Si wafer for 30 s while employing a negative high voltage (5 kV) to the bottom of the wafer (Kim et al. 2022). It was clear that the surface contamination of particles was quite uniform due to their random deposition, as shown in Figure S2.

Secondly, we developed a new system for conducting single-microdroplet cleaning experiments. Traditional nozzle-based spraying systems used for cleaning often lead to multiple droplet impacts, causing significant overlap between droplets and frequent liquid flooding on the surface. This made it challenging to evaluate the cleaning capability of a single microdroplet, resulting in a lack of direct experimental validation for existing cleaning models. Therefore, a primary objective was to minimize droplet overlap after impact, enabling us to distinguish traces of individual droplets.

As depicted in Figure 3, we initiated the process by placing a small drop of D.I. water onto a nylon mesh with dimensions of 1 cm x 1 cm. The pore size of the nylon mesh was as small as 508 µm, allowing a small drop of DI water to rest on top of the nylon mesh without penetrating through. Subsequently, we directed supersonic N_2 gas jets through a two-fluid nozzle, without flowing liquid (Firmansyah et al. 2014; Kaiser et al. 2018), toward the mesh (positioned 1 cm away from the nozzle tip) to generate water droplets. This approach allowed us to control the size and number of microdroplets, almost independently of their impaction velocity, by adjusting the initial volume of the water drop. To monitor the sprayed droplets above the wafer surface, we employed a high-speed camera situated 1.5 cm away from the mesh. This camera, combined with a light source, enabled direct measurements of the diameter and velocity of individual droplets (refer to Figure S3 for more details). For this purpose, we adjusted the camera's frame rate to 20,000 fps.

Figure 4a displays a scatter plot of the data collected for 500 droplets using a high-speed camera in the velocity and diameter domain. This plot indicates that microdroplets with diameters ranging from 10 to 80 µm are observed to move at an average velocity of 16.8 m/s, with a standard deviation of 5.6 m/s, within a range of 5 to 35 m/s. Simultaneously, we collected the water droplets in an organic liquid (1-methyl naphthalene) by placing a petri dish with a diameter of 3 cm containing the organic liquid instead of the wafer, and then visualized the captured droplets using an optical microscope (Leica, DM750M), as demonstrated in Figure S4, for subsequent image analysis using an open source software ImageJ. This allowed us to independently measure the size distribution of the droplets before impact. Recalling the snapshots in Figure S3, it is evident that water droplets are observed to merely move without undergoing further breakup, even at the position of the high-speed camera (1.5 cm away from the nylon mesh). This observation suggests that the water droplets maintain their initial sizes until they are captured in the petri dish. Therefore, we positioned the petri dish 20 cm away

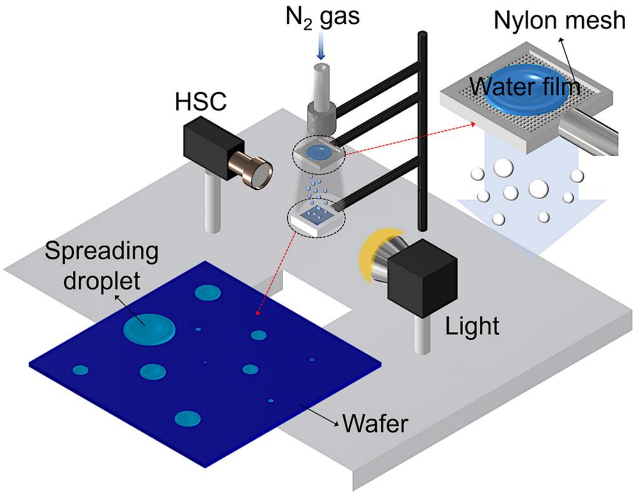

Figure 3. Experimental setup for the single-microdroplet cleaning of the contaminated Si wafer.

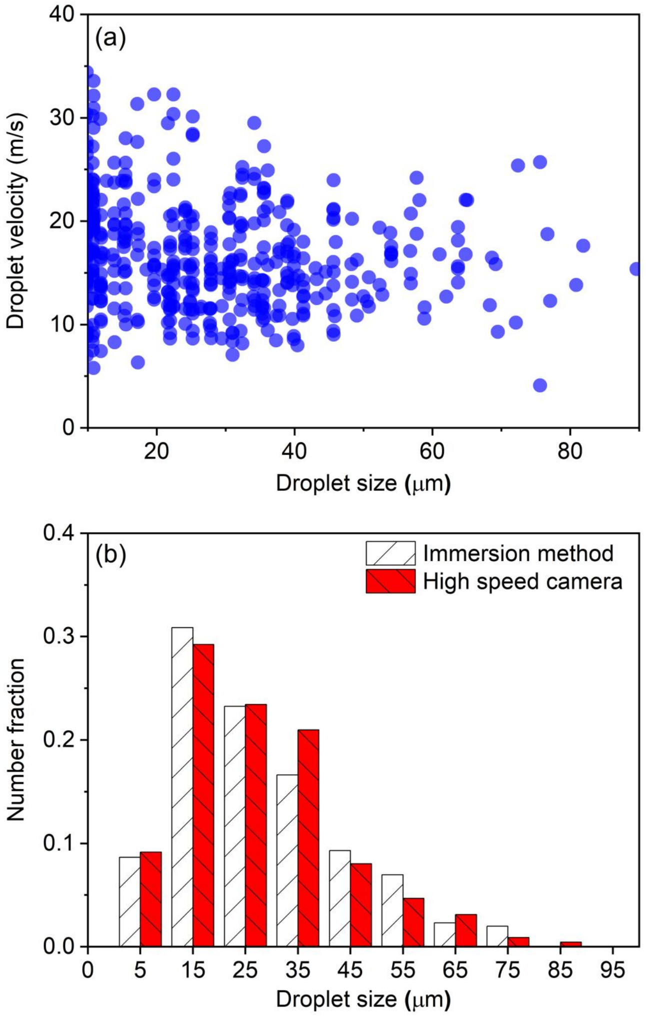

Figure 4. Characteristics of generated microdroplets: (a) scatter plot showing the velocity versus size (diameter) of individual droplets, and (b) number size distribution of the droplets obtained from high-speed camera observations compared with that from the immersion method.

from the mesh, where droplet impacts do not result in any splash of the organic liquid. Moreover, according to the manufacturer (Sigma Aldrich), the density of the organic liquid is 1,001 kg/m^3, which is almost identical to that of water. This allows fine water droplets to remain well suspended upon impact with the organic liquid, without either floating or sinking (refer to Figure S4).

Figure 4b presents the size distribution of droplets converted from Figure 4a, compared to the distribution directly observed from the petri dish. Both methods are confirmed to reasonably measure the size distributions of the droplets, yielding an average droplet diameter of 26.6 µm when using the high-speed camera, which closely aligns with 27.1 µm obtained using the immersion method. A field-emission scanning electron microscope (FE-SEM; ZEISS Supra25) was used to visualize the traces of water droplets on the wafer surface, as illustrated in Figure 3, and to count the nanoparticles existing on the surface both before and after impact. This data will be utilized for subsequent analysis of the effective cleaning diameter (to be explained later) and particle removal efficiency.

3. Results and discussion

3.1. CFD simulations for high-speed impacts of a single microdroplet and its validation

In addition to the simulations in Section 2.2, we conducted similar CFD simulations for microdroplets and compared the results with literature data for further validation. Initially, we calculated the diameter (D) of the spreading liquid film over time (t), and displayed it in a dimensionless form in Figure 5a by plotting β ($= D(t)/D_0$) against t^* ($= tU/D_0$) using a red triangle. As demonstrated in the figure, our simulation results show good agreement with the experimental data from Visser et al. (2015).

Continuing the CFD simulations, we subsequently obtained a set of maximum spreading diameters for a wide range of impaction conditions and compared the simulated $\beta_{\max}$ data with literature data in Figure 5b. Once again, we confirmed that our CFD simulations allow for accurate predictions of maximum spreading diameters in a range of Weber numbers ($10 \le We \le 10,000$). It is noted that our CFD simulations were conducted under the same impaction conditions as those in the experiments of Visser et al. (2012, 2015), specifically focusing on the impact of 50-µm microdroplets. Moreover, we employed the most recent analytical model (Yonemoto and Kunugi 2017) to explore the relationship between $\beta_{\max}$ and We number as

$$\frac{We}{3} - \frac{27}{64}\frac{D_0^2}{t_m^2}\beta_{\max}\frac{We}{Re} - (1\text{-}\cos\overline{\theta})\beta_{\max}^2 + \frac{2t_m}{D_0}\beta_{\max}\sin\overline{\theta} + \frac{1}{3}\frac{\rho g D_0 t_m}{\sigma} + 4 - \frac{4S_{def}}{\pi D_0^2} = 0 \tag{10}$$

where $\overline{\theta}$ is the simple average of the static (θ_0) and dynamic (θ) angles, t_m is the thickness of fully-spread liquid film, and S_{def} represents the free-surface area of the film, approximated as a harmonic average of surface areas between two limiting shapes: a spherical cap for low We numbers vs a flat circular film for high We numbers. By applying the relevant material properties in Table (3) to Equation (10) along with Equations (19)–(21) in the literature, we calculated $\beta_{\max}$ at various impact velocities of a 50-µm water droplet. As a result, we presented the model-predicted results as a solid line in Figure 5b. It is evident that the model effectively tracks the experimental and CFD results in predicting $\beta_{\max}$.

It is also noted that $\overline{\theta} = 55°$ was used for the model prediction, taking into account that $\theta \approx 90°$ from Figure 2b and $\theta_0 = 28°$ from Table 3. For comparison, we included another model prediction, obtained with $\overline{\theta} = 90°$, as a red dotted line in the figure. Notably, the model appears to overpredict $\beta_{\max}$ with a larger value of $\overline{\theta}$ when $We < 10^2$, but its prediction approaches the solid line as We number increases beyond 10^2. According to Yonemoto and Kunugi (2017), when $We < 10^1$, the liquid spreading behavior is subject to the capillary regime, where the contact angle $\overline{\theta}$ has a pronounced effect on $\beta_{\max}$ through the third and fourth terms in Equation (10), as evidenced by Figure 5b. When $We > 10^2$, on the other hand, kinetic energy and viscous dissipation become dominant in Equation (10), leading to a transition into the viscous regime and a scaling law of $\beta_{\max} \propto Re^{1/5} \propto We^{1/10}$. This explains why the two model predictions, as well as our CFD simulation data, approach the guide line representing the scaling law in Figure 5b as the We number increases. It is worth noting that our impact conditions for particle removal mostly lie in the region of $We > 10^2$ (as depicted with solid squares in Figure 5b), suggesting that accurate prediction of $\overline{\theta}$ is less critical for particle removal.

Next, we analyzed the simulated flow fields to investigate the local spreading velocity inside the liquid film as a function of the dimensionless time (t^*) and radial position ($x^* = 2x/D_0$) from the impact point. For instance, Figure 6 displays the local velocity distribution along the vertical position (y) from the surface for two different-sized droplets (10 vs 50 μm) at $t^* = 1$ and $x^* = 0.7$. In the case of the 10-μm droplet impact at $U = 50$ m/s, the velocity distribution profile, represented by a solid line, suggests that at $t^* = 1$, the spherical droplet transforms into a 1-μm thick liquid film at $x^* = 0.7$, and the boundary layer

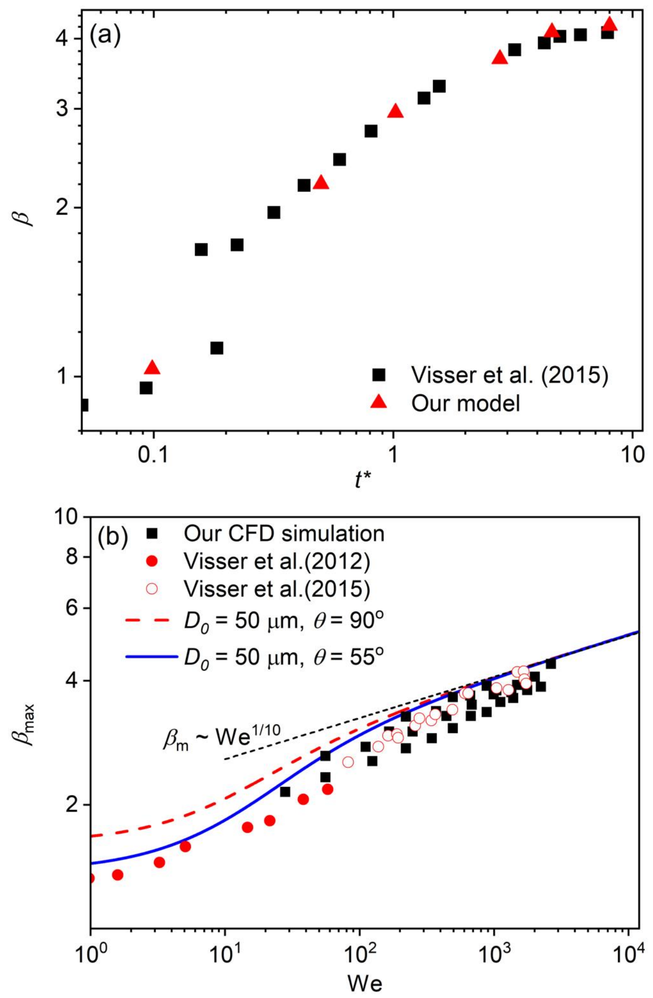

Figure 5. Comparison between the present CFD simulations of microdroplet impaction and literature results in (a) transient evolution of dimensionless diameter ($\beta = D(t)/D_0$) of spreading liquid film, and (b) the simulated β_{max} data under various We number conditions.

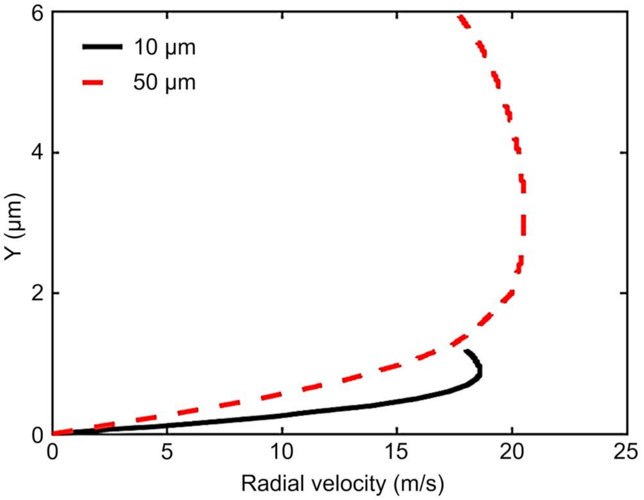

Figure 6. Local spreading velocity distribution along the vertical position (Y) for two different-sized droplets at $t^* = 1$ and $x^* = 0.7$.

almost fully develops from the surface. Meanwhile, the 50-μm droplet, impacted at the same velocity, forms a relatively thicker liquid film, resulting in a thicker boundary layer. This reaffirms that the local spreading velocity (V_R) at the center of a target nanoparticle is much smaller than both the spreading velocity at the leading edge of the liquid film and the impaction velocity (U) of the droplet.

3.2. Predictions of effective cleaning diameter

Continuing the CFD simulations involving droplets of different sizes and impact velocities, we collected datasets of flow fields at various times and positions. Referring back to Figure 5a, it is worth noting that β initially rises rapidly and then levels off, indicating a continual decrease in the spreading velocity for the majority of the time ($t^* > 0.1$). We observed that local velocity data (V_R) at the height of particle center undergoes similar changes over time in response to the film spreading velocity. From the collected dataset, we extracted V_R data along a horizontal line at $y = d_p/2$ (representing the height of the particle center) at every time step. Subsequently, we identified the maximum value in the V_R data ($V_{R,\max}$) and its corresponding radial position ($x_{R,\max}$) at each time. We also observed that the maximum velocity $V_{R,\max}$ gradually decreases over time, while its radial position moves away from the point of impact. Regarding this, we determined when $V_{R,\max}$ begins to fall below a critical value by monitoring, leading to $\sum M < 0$ in Equation (9). In fact, the maximum value of $x_{R,\max}$ observed at that time becomes half of the effective cleaning diameter ($D_{removal}$). Since $D_{removal}$ is always smaller than the maximum spreading diameter, $D_{\max}$, the term $D_{removal}$ was normalized by the corresponding $D_{\max}$ to define the intrinsic particle removal efficiency (PRE) of a single droplet as $PRE = A_{removal}/A_{\max} = D^2_{removal}/D^2_{\max}$.

In Figure 7, we plotted the area ratio $A_{removal}/A_{\max}$ against the impaction velocity of droplets, varying the droplet diameter from 10 to 50 µm. It was observed that droplets across all size ranges exhibit higher cleaning area ratios as their velocity increases, which is consistent with the general understanding that higher-speed impaction is advantageous for particle removal (Ibrahim, Dunn, and Brach 2003; Xu et al. 2009). Importantly, smaller droplets consistently showed higher area ratios compared to larger ones at the same velocity, suggesting their greater efficiency in removing 20-nm particles. This observation finds support in Figure 6, where the local spreading velocity (involving V_R) of a 10-µm droplet was higher than that of a 50-µm droplet particularly near the surface. However, this should not be interpreted as smaller droplets clean a larger area. Referring to Figure 7, it is evident that larger droplets can indeed cover a larger cleaning area ($A_{removal}$) by multiplying the area ratio by $A_{\max}$, albeit at the expense of reduced particle removal efficiency.

Beyond the ratio $A_{removal}/A_{\max}$, readers might have a stronger interest in a priori prediction of $D_{removal}$ based on droplet impaction conditions, because $D_{removal}$ itself defines the intrinsic capability of an individual microdroplet upon impaction for particle removal. For this reason, we transformed Figure 7 into a contour plot of $D_{removal}$ in a two-dimensional space defined by the diameter and velocity of droplets. Furthermore, we performed CFD simulations, akin to those shown in Figure 7, for the removal of 50-nm particles in order to comparatively analyze the contour plot.

Figure 8a shows the $D_{removal}$ contour for the removal of 20-nm Ti particles, while Figure 8b contrasts the contour map for the case of 50-nm Ti particles. In both figures, there are two dash lines, each representing a constant value of $D_{removal}$ at 25 µm or 50 µm. In Figure 8a, the dotted lines, resembling colorful contour bands, look like a reciprocal function with negative slopes, indicating an inverse relationship between the diameter and velocity of droplets in achieving a specific but fixed cleaning diameter ($D_{removal}$). For instance, larger droplets are required to impact at lower velocities, whereas smaller droplets need to impact at higher velocities to yield the same cleaning diameter. This clearly suggests that both the diameter and velocity of droplets are crucial parameters for effectively removing 20-nm particles. In contrast, the dotted lines in Figure 8b appear relatively vertical with steeper negative slopes. The aqua blue-to-red zone notably extends downward (toward lower velocities) compared to Figure 8a. This observation suggests that the droplet diameter has a more pronounced effect on the removal of 50-nm particles than on the removal of 20-nm particles. For instance, when maintaining the impact velocity at $U = 20$ m/s, increasing the droplet diameter up to 50 µm leads to more pronounced color changes along an imaginary horizontal line in Figure 8b. This indicates that the maximum value of $D_{removal}$ reaches 139 µm, significantly surpassing the value (86 µm) in Figure 8a. This seems qualitatively consistent with Snow et al. (2013)'s experimental report that 40-µm droplets are more advantageous than 22-µm droplets at the same velocity for removing 78-nm particles (refer to Figure 3.23 in the literature). However, it should be noted that their experiment involved multiple droplet impacts, leading to the formation of a liquid layer on top of the wafer surface, which could affect the cleaning performance of droplets. Due to these disparities,

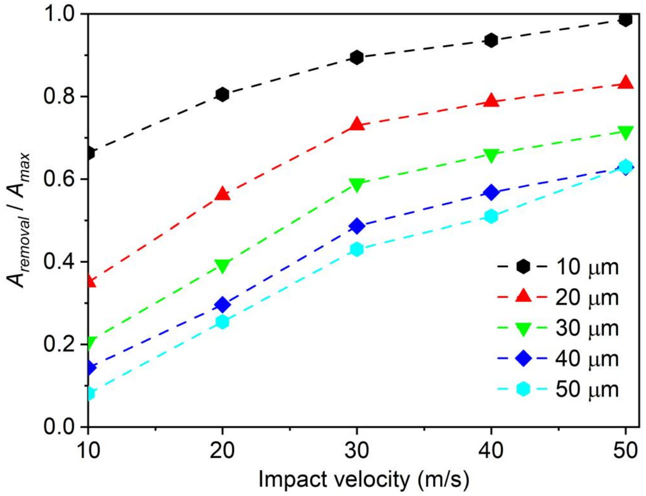

Figure 7. Changes in the effective cleaning area ratio $(A_{removal}/A_{\max})$ with varying the size and impaction velocity of droplets.

direct comparisons between our single droplet-based analysis and the existing literature may raise questions.

3.3. Experimental evidence for the effective cleaning diameter of a single droplet

Following the procedures outlined in Section 2.3, we conducted additional experiments to validate our model's predictions of the cleaning diameters. Figure 9a presents a FE-SEM image illustrating the traces left by individual droplets upon impacting the contaminated wafer surface. The figure notably showcases numerous visible circular traces, together with a few instances of overlapping circles that remain distinguishable, indicating the anticipated reduction in overlap between spreading droplets. Each non-overlapping circular mark represents the cleaned area by an individual droplet. To confirm this hypothesis, we magnified an independent circular trace, as depicted in Figure 9b. Within the circular mark, notably fewer particles are present compared to its surroundings, which enables a clear delineation of its boundary and facilitating diameter measurement. Readers might wonder: where did the particles inside the circular mark go? To address this question, we magnified three distinct sites labeled 'A', 'B', and 'C' in Figure 9b, presenting each in Figures 9c–e, respectively.

Comparing Figures 9d and e, one can notice a distinct absence of darker and larger spots (observed in site 'C') within site 'B', along with a substantial reduction in their overall population. This indicates that larger particles are mostly removed by the impact of a single droplet, while some smaller ones may remain. On the other hand, Figure 9c elucidates the event occurring in the boundary region (site 'A'). Particles positioned right at the edge of the circular trace appear notably darker and larger, compared to those located farther from the boundary such as in site 'C'. This observation suggests that particles initially located inside the boundary aren't completely removed; instead, they seem to migrate toward the boundary after detaching from the surface before resettling on it. Specifically, the presence of elongated structures in Figure 9c suggests that particles detached within the circular trace are likely agglomerated during their resettlement near the boundary.

To quantitatively analyze these observations, we measured the diameters of all particles visible in Figures 9d and e using open-source software (ImageJ). Subsequently, we compared the resulting (number) size distributions of particles remaining in the two sites: site 'B' and 'C'. In Figure 10a, the profile represented by solid circles illustrates the size distribution of pristine particles outside the circular trace (site 'C'), while the profile indicated by solid triangles depicts the size distribution of particles within the circular trace (site 'B'). As a result, we confirmed that particles larger than 40 nm are nearly entirely removed by the impact, although a small fraction of particles sized between 5 and 35 nm remain.

In Figure 10b, we compared the size distribution of particles near the boundary (site 'A') with that of the pristine particles in site 'C'. Interestingly, the boundary particles, especially when $d_p > 40\,\text{nm}$, display slightly larger populations than the pristine particles of the same size, indicating an influx of particles from the boundary's interior. However, the observed population increase is not as substantial as expected based on the number of removed particles shown in Figure 10a. Moreover, the total population of boundary particles per unit area of the surface is smaller than that

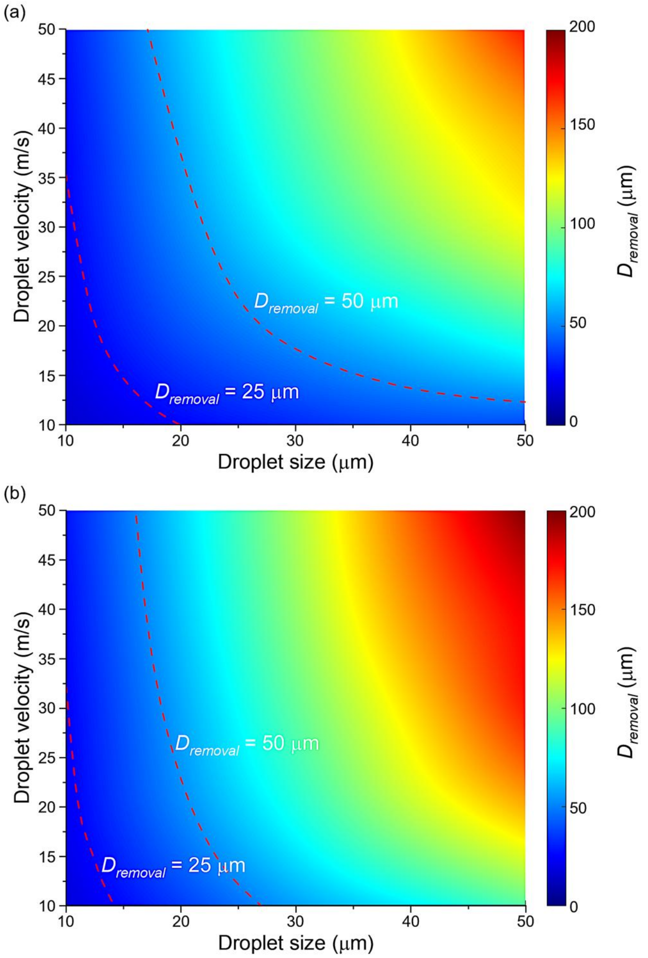

Figure 8. Contour plots of $D_{removal}$ as a function of droplet size and velocity for the removal of (a) 20-nm and (b) 50-nm Ti particles.

of pristine particles, even with the influx of removed particles. One possible explanation might involve the agglomeration of incoming particles with existing ones during their resettlements, along with the image analysis approach that treated elongated agglomerates (see Figure 9c) as single particles with equal projected areas.

Therefore, in Figure 10c, we plotted projected areas of agglomerates (or spherical particles) against their area-equivalent diameters with the aim of elucidating the number of elementary particles comprising each agglomerate. As expected, the figure shows that the projected-area size distribution more accurately portrays the migration of particles from the circular trace. Particularly noteworthy is the significant increase in the total projected area covered by all particles in the boundary in comparison to that of pristine particles. This disparity signifies the influx of particles after detachments.

To the best of our knowledge, Figures 9–10 present the first experimental data to assess the cleaning capability of a single microdroplet. It is important to note that this observation was made possible only by minimizing the number of sprayed droplets. In summary, the single microdroplet we examined demonstrates an ability to remove sub-100 nm particles with an overall particle removal efficiency (PRE) of 72%. Notably, removing smaller particles proves more challenging than larger ones, resulting in a 55% PRE for 15 nm particles. In contrast, previous studies on nozzle-based cleaning typically involved spraying large amounts of liquid over an extended duration. Consequently, these processes essentially lead to the formation of a thick liquid film, followed by continuous liquid flooding on the surface. This enables the continuous removal of detached particles from the surface by flowing water. In general, therefore, the primary concern lies not in the ultimate removal of particles but rather in the reduction in particle removal efficiency due to the cushioning effect of thick liquid film.

Now, it is important to note that the data presented in this section mainly reflects the outcomes of a specific individual droplet rather than the collective

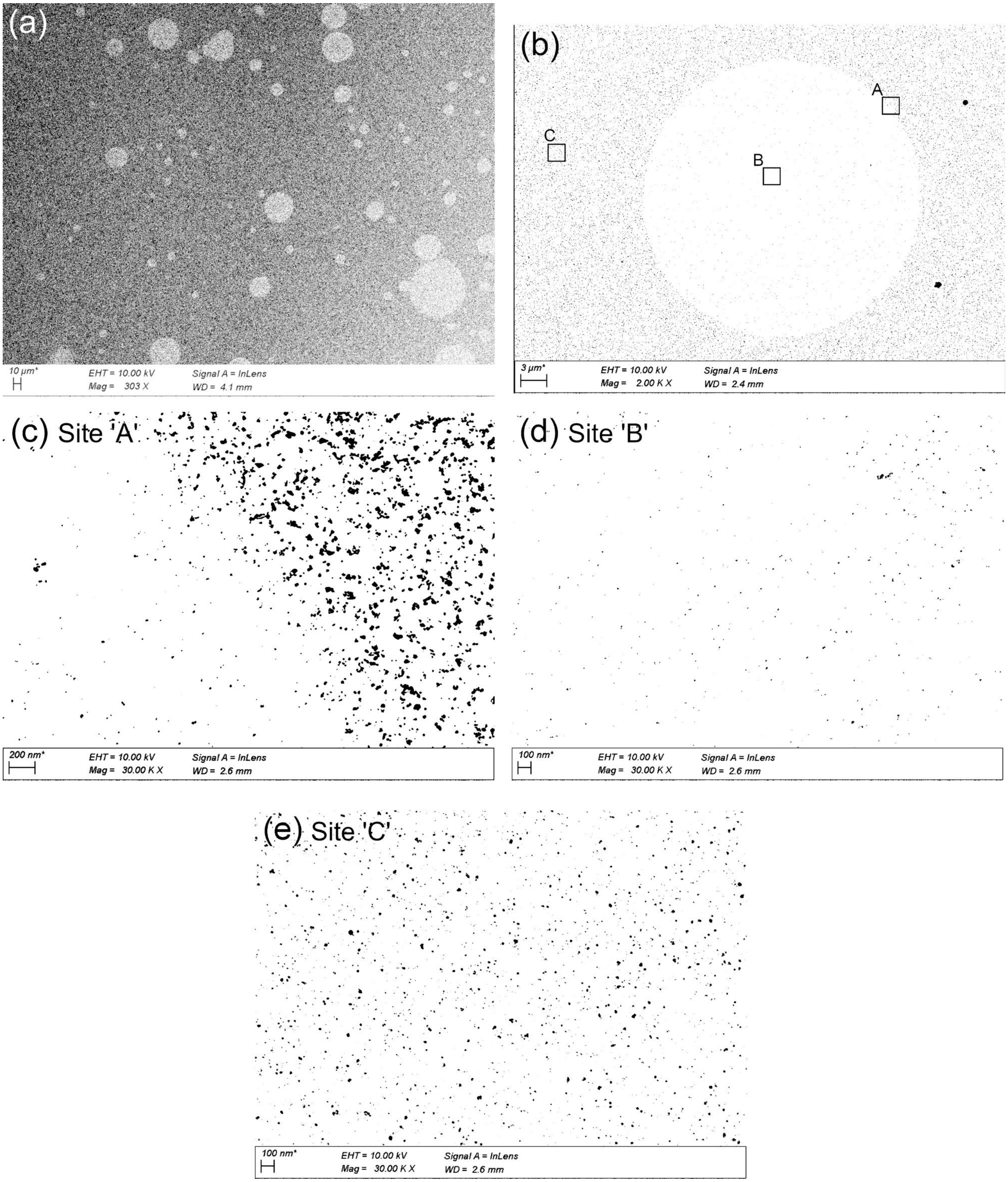

Figure 9. Field-emission scanning electron microscope (FE-SEM) images of (a) contaminated wafer surface after droplet impact at a low magnification, (b) the area involving a single circular trace, (c) the near-boundary area of the trace magnified for site 'A', (d) the interior of the trace magnified for site 'B', and (e) the far field from the boundary magnified for site 'C'.

behavior of all droplets. Referring back to Figure 6a, the droplets exhibit significant variations in sizes and velocities upon impact, resulting in markedly diverse cleaning traces on the wafer surface and leading to variations in $D_{removal}$ and PRE. Consequently, it becomes challenging to directly correlate each droplet trace with its impact condition (in terms of D_0 and U). To circumvent this complexity, we instead focused on the circular traces themselves (as shown in Figure 9a) which provide an experimental dataset for $D_{removal}$.

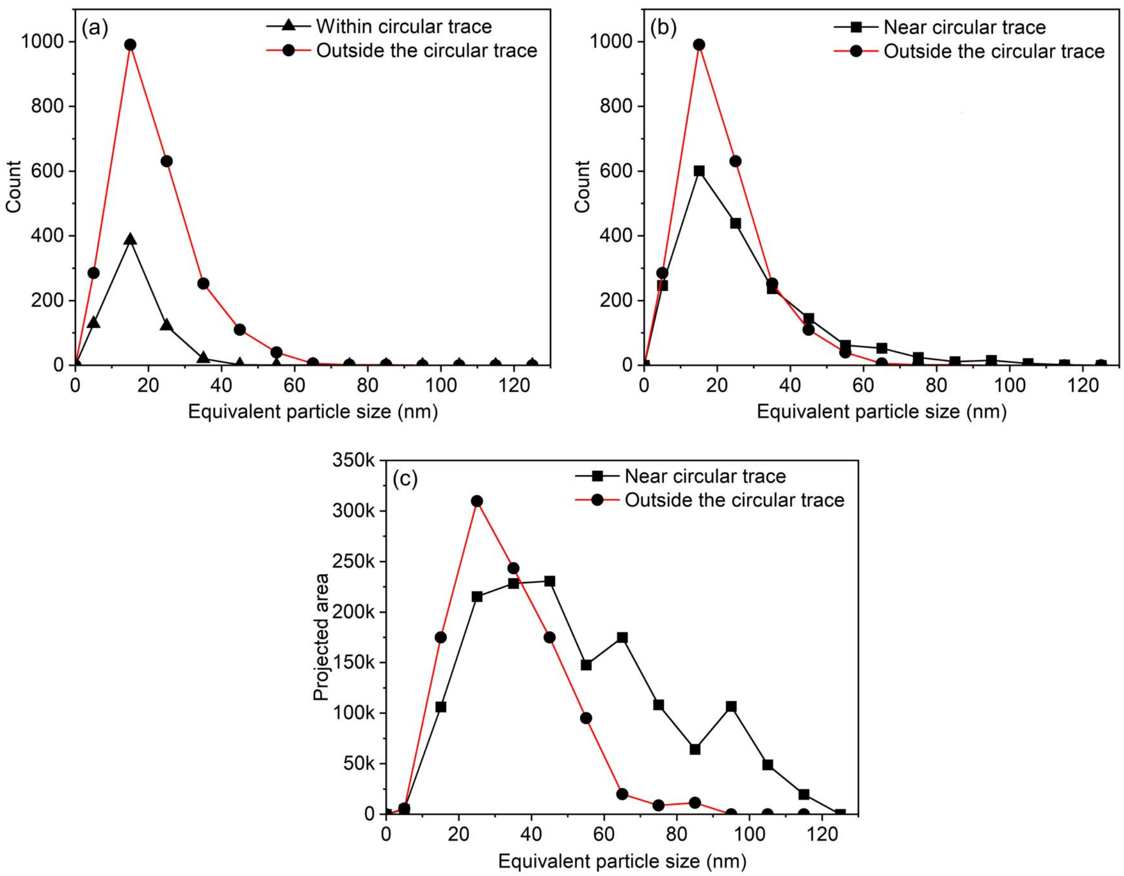

Figure 10. Comparison between the number size distributions of particles remaining on the sites of interest: (a) outside and within the circular trace, and (b) near the boundary and outside circular trace; and (c) comparison of area size distributions of particles between near the boundary and outside the circular trace.

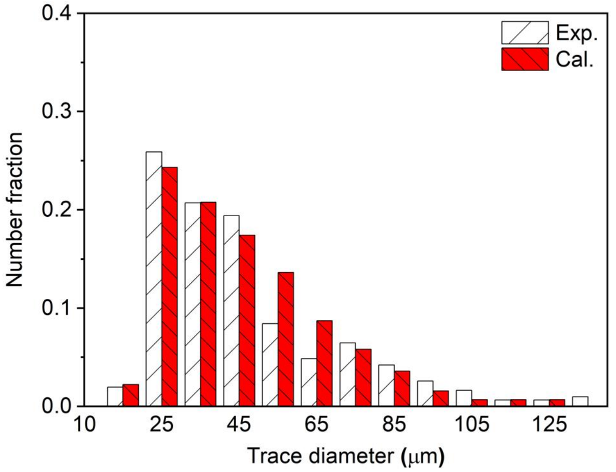

Figure 11. Histograms of two independent datasets for $D_{removal}$, comparison between experimental and simulation results.

Concurrently, using the dataset of D_0 and U from Figure 6a, we calculated $D_{removal}$ for each droplet impact employing our cleaning model. This approach allowed us to establish two independent datasets for $D_{removal}$, enabling a direct comparison of their histograms in Figure 11. Finally, we confirmed a strong agreement between the model predictions and the experimental data across the entire range of $D_{removal}$.

4. Conclusions

In this study, we conducted CFD simulations and experiments to examine diverse dropwise impactions for cleaning particulate contaminants with an average diameter of 20 nm on a wafer surface. Initially, we simulated the transient spreading behaviors of large water droplets under free-fall conditions, validating the simulation results against literature values and our experimental data. Subsequently, we analyzed the spreading flow field of microdroplets to extract the local velocity at the position of the attached nanoparticle. This data was then integrated into an existing model to determine the effective cleaning diameter. To encompass the entire range of impact conditions, we repeated this calculation process to generate a contour plot capable of predicting the effective cleaning diameter for specific impaction conditions. Simultaneously, we conducted single-droplet cleaning experiments for the first time, collecting the experimental dataset for the effective cleaning diameters of individual droplets. Upon comparing the two datasets, we observed a strong agreement between the experimental data and our model predictions based on the local velocity data. Moreover, the observation that particles solely shift in position on the surface upon the impact of a single droplet presents an intriguing future prospect: leveraging a minimal amount of spray, adequate for removing detached particles from the surface but prior to forming a thick liquid film, becomes essential to maximize the particle removal efficiency of microdroplets.

Disclosure statement

No potential conflict of interest was reported by the author(s).

Funding

This research was supported by Basic Science Research Program through the National Research Foundation of Korea (NRF) funded by the Ministry of Education (No. 2020R1A2C2011634) and also by a Korea Institute of Energy Technology Evaluation and Planning (KETEP) grant funded by the Korea government (MOTIE) (20214000000140, Graduate School of Convergence for Clean Energy Integrated Power Generation).

References

Bergström, L. 1997. Hamaker constants of inorganic materials. *Adv. Colloid Interface Sci.* 70:125–169. doi:10.1016/S0001-8686(97)00003-1.

Burdick, G. M., N. S. Berman, and S. P. Beaudoin. 2005. Hydrodynamic particle removal from surfaces. *Thin Solid Films* 488 (1–2):116–123. doi:10.1016/j.tsf.2005.04.112.

Cho, Y., H. Choi, S. Mo, and T. Kim. 2020. Removal of nano-sized surface particles by CO2 gas cluster collisions for dry cleaning. *Microelectron. Eng.* 234:111438. doi:10.1016/j.mee.2020.111438.

Choudhury, R., J. Choi, S. Yang, Y. J. Kim, and D. Lee. 2017. Maximum spreading of liquid drop on various substrates with different wettabilities. *Appl. Surf. Sci.* 415: 149–154. 10.1016/j.apsusc.2016.12.195.

Derjaguin, B. V., V. M. Muller, and Y. P. Toporov. 1975. Effect of contact deformations on the adhesion of particles. *J. Colloid Interface Sci.* 53 (2):314–326. doi:10.1016/0021-9797(75)90018-1.

Engineering ToolBox. 2004. Retrieved December 1, 2023, from https://www.engineeringtoolbox.com/water-dynamic-kinematic-viscosity-d_596.html; https://www.engineeringtoolbox.com/water-density-specific-weight-d_595.htm; https://www.engineeringtoolbox.com/water-surface-tension-d_597.html

Firmansyah, D. A., R. Kaiser, R. Zahaf, Z. Coker, T. Y. Choi, and D. Lee. 2014. Numerical simulations of supersonic gas atomization of liquid metal droplets. *Jpn. J. Appl. Phys.* 53 (5S3):05HA09. doi:10.7567/JJAP.53.05HA09.

Hanson, B. 1995. *The selection and use of titanium: A design guide*. London: Institute of Materials, 44.

Henry, C., and J. P. Minier. 2014. Progress in particle resuspension from rough surfaces by turbulent flows. *Prog. Energy Combust. Sci.* 45:1–53. doi:10.1016/j.pecs.2014.06.001.

Hong, S., J. Kim, J. Won, N. Qureshi, S. Chae, Y. Wada, H. Hiyama, S. Hamada, and T. Kim. 2019. A water polishing process to improve ceria abrasive removal. *ECS J. Solid State Sci. Technol.* 8 (8):P430–P436. doi:10.1149/2.0171908jss.

Hung, Y. L., M. J. Wang, Y. C. Liao, and S. Y. Lin. 2011. Initial wetting velocity of droplet impact and spreading: Water on glass and parafilm. *Colloids Surf. A* 384 (1-3): 172–179. doi:10.1016/j.colsurfa.2011.03.061.

Ibrahim, A. H., P. F. Dunn, and R. M. Brach. 2003. Microparticle detachment from surfaces exposed to turbulent air flow: Controlled experiments and modeling. *Aerosol Sci.* 34 (6):765–782. doi:10.1016/S0021-8502(03)00031-4.

Iwasaki, A., A. Higuchi, K. Komori, M. Sato, and H. Shirakawa. 2015. Dual-fluid spray process for particle and fluorocarbon-polymer removal in BEOL applications. *ECS Trans.* 69 (8):199–205. doi:10.1149/06908.0199ecst.

Johnson, K. L., K. Kendall, and A. Roberts. 1971. Surface energy and the contact of elastic solids. *Proc. R. Soc. Lond. A Math. Phys. Sci.* 324 (1558):301–313. doi:10.1098/rspa.1971.0141.

Jung, S., and I. M. Hutchings. 2012. The impact and spreading of a small liquid drop on a non-porous substrate over an extended time scale. *Soft Matter.* 8 (9):2686–2696. doi:10.1039/c2sm06565g.

Kaiser, R., C. Li, S. Yang, and D. Lee. 2018. A numerical simulation study of the path-resolved breakup behaviors of molten metal in high-pressure gas atomization: With emphasis on the role of shock waves in the gas/molten metal interaction. *Adv. Powder Technol.* 29 (3):623–30. doi:10.1016/j.apt.2017.12.003.

Kern, W. 1990. The evolution of silicon wafer cleaning technology. *J. Electrochem. Soc.* 137 (6):1887–1892. doi:10.1149/1.2086825.

Kim, S., K. Park, C. Choi, M. Y. Ha, and D. Lee. 2022. Removal of ultrafine particles in a full-scale two-stage electrostatic precipitator employing a carbon-brush ionizer for residential use. *Build. Environ.* 223:109493. doi:10.1016/j.buildenv.2022.109493.

Kondo, T., and K. Ando. 2019. Simulation of high-speed droplet impact against a dry/wet rigid wall for understanding the mechanism of liquid jet cleaning. *Phys. Fluids* 31 (1):013303. doi:10.1063/1.5079282.

Lee, J. B., D. Derome, A. Dolatabadi, and J. Carmeliet. 2016. Energy budget of liquid drop impact at maximum spreading: Numerical simulations and experiments. *Langmuir* 32 (5):1279–1288. doi:10.1021/acs.langmuir.5b03848.

Lee, H., S. You, P. V. Pikhitsa, J. Kim, S. Kwon, C. G. Woo, and M. Choi. 2011. Three-dimensional assembly of nanoparticles from charged aerosols. *Nano Lett.* 11 (1):119–124. doi:10.1021/nl103787k.

Liu, X., X. Zhang, and J. Min. 2019. Maximum spreading of droplets impacting spherical surfaces. *Phys. Fluids* 31 (9): 092102. doi:10.1063/1.5117278.

Moram, M. A., Z. H. Barber, C. J. Humphreys, T. B. Joyce, and P. R. Chalker. 2006. Young's modulus, Poisson's ratio, and residual stress and strain in (111)-oriented scandium nitride thin films on silicon. *J. Appl. Phys.* 100 (2):023514. doi:10.1063/1.2217106.

Ock, Y., J. Kim, I. Choi, D. S. Kim, M. Choi, and D. Lee. 2018. Size-independent unipolar charging of nanoparticles at high concentrations using vapor condensation and its application for improving DMA size-selection efficiency. *J. Aerosol Sci.* 121:38–53. doi:10.1016/j.jaerosci.2018.04.007.

Okorn-Schmidt, H. F., F. Holsteyns, A. Lippert, D. Mui, M. Kawaguchi, C. Lechner, P. E. Frommhold, T. Nowak, F. Reuter, M. B. Piqué, et al. 2014. Particle cleaning technologies to meet advanced semiconductor device process requirements. *ECS J. Solid State Sci. Technol.* 3 (1): N3069–N3080. doi:10.1149/2.011401jss.

Pasandideh-Fard, M., Y. M. Qiao, S. Chandra, and J. Mostaghimi. 1996. Capillary effects during droplet impact on a solid surface. *Phys. Fluids* 8 (3):650–659. doi:10.1063/1.868850.

Riboux, G., and J. M. Gordillo. 2014. Experiments of drops impacting a smooth solid surface: A model of the critical impact speed for drop splashing. *Phys. Rev. Lett.* 113 (2): 024507. doi:10.1103/PhysRevLett.113.024507.

Roisman, I. V., R. Rioboo, and C. Tropea. 2002. Normal impact of a liquid drop on a dry surface: model for spreading and receding. *Proc. R. Soc. Lond. A* 458 (2022): 1411–1430. doi:10.1098/rspa.2001.0923.

Sato, M., K. Sotoku, K. Yamaguchi, T. Tanaka, M. Kobayashi, and S. Nadahara. 2011. Analysis on threshold energy of particle removal in spray cleaning technology. *ECS Trans.* 41 (5):75–82. doi:10.1149/1.3630829.

Seike, Y., K. Miyachi, T. Shibata, Y. Kobayashi, S. Kurokawa, and T. Doi. 2010. Silicon wafer cleaning using new liquid aerosol with controlled droplet velocity and size by rotary atomizer method. *Jpn. J. Appl. Phys.* 49 (6R):066701. doi:10.1143/JJAP.49.066701.

Snow, J. T., M. Sato, and T. Tanaka. 2013. Dual-fluid spray cleaning technique for particle removal. In *Developments in surface contamination and cleaning*, eds. R. Kohli and K. L. Mittal, vol. 6, 109–38. Oxford, UK: Elsevier. doi:10.1016/B978-1-4377-7879-3.00003-0.

Soltani, M., and G. Ahmadi. 1994. On particle adhesion and removal mechanisms in turbulent flows. *J. Adhes. Sci. Technol.* 8 (7):763–785. doi:10.1163/156856194X00799.

Tan, H. 2017. Numerical study on splashing of high-speed microdroplet impact on dry microstructured surfaces. *Comput. Fluids* 154:142–166. doi:10.1016/j.compfluid.2017.05.014.

Visser, C. W., P. E. Frommhold, S. Wildeman, R. Mettin, D. Lohse, and C. Sun. 2015. Dynamics of high-speed micro-drop impact: Numerical simulations and experiments at frame-to-frame times below 100 ns. *Soft Matter.* 11 (9):1708–1722. doi:10.1039/C4SM02474E.

Visser, C. W., Y. Tagawa, C. Sun, and D. Lohse. 2012. Microdroplet impact at very high velocity. *Soft Matter* 8 (41):10732–10737. doi:10.1039/c2sm26323h.

Voinov, O. V. 1976. Hydrodynamics of wetting. *Fluid Dyn.* 11 (5):714–721. doi:10.1007/BF01012963.

Wang, X. D., D. J. Lee, X. F. Peng, and J. Y. Lai. 2007. Spreading dynamics and dynamic contact angle of non-Newtonian fluids. *Langmuir* 23 (15):8042–8047. doi:10.1021/la0701125.

Wang, M. J., F. H. Lin, Y. L. Hung, and S. Y. Lin. 2009. Dynamic behaviors of droplet impact and spreading: Water on five different substrates. *Langmuir* 25 (12): 6772–6780. doi:10.1021/la9002862.

Xu, W., J. Luo, J. Qin, and Y. Zhang. 2017. Maximum deformation ratio of droplets of water-based paint impact on a flat surface. *Coatings* 7 (6):81. doi:10.3390/coatings7060081.

Xu, K., S. Pichler, K. Wostyn, G. Cado, C. Springer, G. W. Gale, M. Dalmer, P. W. Mertens, T. Bearda, E. Gaulhofer, et al. 2009. Removal of nano-particles by aerosol spray: Effect of droplet size and velocity on cleaning performance. *SSP.* 145–146:31–34. doi:10.4028/www.scientific.net/SSP.145-146.31.

Yonemoto, Y., and T. Kunugi. 2017. Analytical consideration of liquid droplet impingement on solid surfaces. *Sci. Rep.* 7 (1):2362. doi:10.1038/s41598-017-02450-4.

You, S., and M. P. Wan. 2013. Mathematical models for the van der Waals force and capillary force between a rough particle and surface. *Langmuir* 29 (29):9104–9117. doi:10.1021/la401516m.

Zoeteweij, M. L., J. C. J. Van der Donck, and R. Versluis. 2009. Particle removal in linear shear flow: Model prediction and experimental validation. *J. Adhes. Sci. Technol.* 23 (6):899–911. doi:10.1163/156856109X411247.